Green Chemistry

COMMUNICATION

View Article Online
View Journal | View Issue

Cite this: *Green Chem.*, 2018, **20**, 978

Received 22nd December 2017,
Accepted 6th February 2018

DOI: 10.1039/c7gc03822d

rsc.li/greenchem

Ag photoionization-induced single-pass assembly of Ag_2S nanodots in flowing thiol droplets†

Bijay Kumar Poudel,[a] Kyung-Oh Doh*[b] and Jeong Hoon Byeon *[a]

Photoinduced assembly of Ag_2S nanodots with surface thiolates was achieved in a single-pass gas stream configuration. Ag nanoagglomerates were converted into aligned Ag_2S nanodots without hydrothermal reaction, separation, or purification procedures. The proposed route to fabricate hybrid nanodroplets containing Ag nanoagglomerates and 1-hexanethiol resulted in electrostatic interactions between Ag surfaces and thiol groups to assemble Ag_2S nanodots. Photoirradiation (185 nm wavelength UV light) onto the nanodroplets induced electron detachments from Ag *via* photons (photon energy: 6.2 eV) reaching the Ag (work function: 4.3 eV) surfaces. The positively charged Ag surfaces interacted with the negatively charged surrounding thiol groups, resulting in the formation of Ag_2S nanodots. Continuous photoirradiation for 6.4 s resulted in complete phase transfer; thus, inducing the isolation of the nanodots (*i.e.*, resulting in an aligned structure of the nanodots without random aggregation) by conjugated surface thiolates. The nanodots were stably dispersible for near-infrared-radiation-induced fluorescence bioimaging without significant cytotoxic effects; furthermore, merging the nanodots with TiO_2 nanoparticles significantly enhanced photocurrent generation under simulated solar irradiation. The photoinduced assembly demonstrates a new feasible safe-by-design platform to continuously produce photoresponsive nanodots without optimization concerning chemically efficient and environmentally benign concepts.

The "size-effect" of metallic nanoparticles (NPs) (*e.g.*, quantum dots and nanocatalysts) has driven rapid developments in physics and chemistry as well as in materials science. Even though the size of NPs is the major parameter used to control or tune their physicochemical properties, chemical surface modification or coordination of the NPs has only recently been extensively studied in the nanoscience and nanotechnology fields.[1] In particular, various surface modifications have been made to improve the targeting, protecting, circulating, or drug/protein loading of NPs in numerous theranostic applications, including toxicological studies.[2–4] More recently, surface modification has been further considered as a safe-by-design approach for metallic NPs to reduce their toxic effects without substantial changes in the original NPs' properties and functionalities.[5,6]

The safe-by-design approach to metallic NPs implies an alignment between their functionality and safety; thus, the safe-by-design approach generally requires precise surface modification of NPs to achieve safety or inertness toward human health and the environment while maintaining the NPs' desired functionalities.[7] Metallic NPs subjected to sulfidation or thiolation have been demonstrated to exhibit negligible cytotoxicity and apoptosis and to generate few reactive oxygen species (ROS) while simultaneously displaying promising fluorescence emission in bioimaging.[8–11] Controlled surface oxidation and metal doping have also been used to reduce the toxic effects of metallic NPs widely used in industry *via* a significant decrease in the dissolution of metal ions.[5] Most approaches to producing safer metallic NPs are related to passivating them with biocompatible polymers to control their direct exposure or contact with biological systems. More recently, researchers have developed different strategies to prepare safer NPs as next-generation nanomaterials by changing the structure of NPs instead of passivating them.[6]

The use of precisely surface-coordinated assemblies to produce functionalized metallic NPs has recently been investigated,[12,13] where researchers specifically attempted to achieve or design safer NPs for theranostic applications.[14,15] Even though precise control of the NP surfaces could achieve the desired functionality for specific applications, more complicated chemical processes are needed. Most surface modifications are based on multistep batch chemical reactions, which require separations, purifications, or templates. In this regard, assemblies of desired NPs in the gas phase have drawn

[a]*School of Mechanical Engineering, Yeungnam University, Gyeongsan 38541, Republic of Korea. E-mail: postjb@yu.ac.kr*
[b]*Department of Physiology, Yeungnam University, Daegu 42415, Republic of Korea. E-mail: kodoh@ynu.ac.kr*

†Electronic supplementary information (ESI) available. See DOI: 10.1039/c7gc03822d

great interest since the atomically precise production of carbonaceous nanomaterials (*e.g.*, C_{60})[16] because the use of gas phase assemblies can reduce the number of reaction steps and the amount of generated waste; this approach has even been demonstrated to be suitable for continuous production.[17] However, the range of producible NPs is limited because of the high operating temperatures. Mostly metals, metal oxides, and carbon NPs are used in gas phase processes; thus, a post-treatment process is generally required to modify their surfaces. Moreover, because of their fast thermal behavior, gas phase processes commonly produce nanoagglomerates of several primary particles that are very difficult to separate from the agglomerates.[18]

The further advancement of gas phase NP synthesis methods requires the development of a scientifically straightforward, easily controllable, and continuous process to achieve the conceptually near-impossible goals of assembling safe, aligned, and functionalized nanodots in an ambient single-phase gas stream. Unlike conventional routes to assemble functional nanodots, the gas-phase assembly not only can continuously produce nanodots but also can reduce multiple hydrothermal reactions, purifications, or separations as well as unwanted process waste. On this account, solvent-free approaches have recently been conducted to secure feasibility for luminescence applications.[19,20] Herein, we designed a gas phase reaction route to produce aligned Ag_2S nanodots that do not exhibit significant cytotoxic effects because of their sulfur-substituted structure with surface thiolates. Because of their unique optical and environmentally benign properties, Ag_2S nanodots have recently attracted attention in bioimaging and photovoltaic applications.[14,21,22] Fortunately, some Ag_2S nanodots that do not exhibit significant cytotoxicities even in the absence of PEGylation are available for bioimaging.[23] However, the coordination of surface thiolates on Ag NPs has been reported to be more difficult and complicated than that on Au NPs, although the surface chemistry of Ag NPs is similar to that of Au NPs.[1] In the present work, changing the matrix and alignment of Ag nanoagglomerates was achieved by exploiting the photoionization phenomenon of Ag particles in a thiol droplet, where the positively charged Ag surfaces are favorable for binding coexisting thiol groups (Fig. S1, ESI†). In particular, photon (6.2 eV) irradiation of an Ag (work function: 4.3 eV) surface induces successive electron detachment from the primary particles of Ag nanoagglomerates; thus, electrostatic binding is induced between the positively charged Ag (Ag^+) surfaces and the negatively charged thiol groups (SH^-), resulting in the formation of Ag_2S nanodots (Fig. 1) within 7 s of photoirradiation. Even though a photoinduced assembly to produce metal sulfide NPs was recently proposed as a low-temperature controllable reaction platform,[24] it is still based on batch wet–chemistry; thus, the development of mild and continuous reaction platforms will be required for its generalization. The method proposed in the present work requires neither multistep wet chemistries nor separations, purifications, high temperatures, or post-treatments for surface modification and realignment of Ag nanoagglomerates. The assembled nanodots were subjected to *in vitro* assays to evaluate their efficacy in near-infrared (NIR) photoluminescence (PL) imaging along with their biocompatibility. The nanodots were further incorporated with TiO_2 NPs to assemble $Ag_2S@TiO_2$ nanocomposites in a single-pass gas stream, and the resulting nanocomposites exhibited enhanced photocurrent generation under simulated solar-light irradiation.

Irradiation under 185 nm UV light initiates conversion from Ag nanoagglomerates into Ag_2S nanodots *via* photoionization of Ag, which imparts the Ag with an affinity for the coexisting negatively charged thiol groups in a droplet (*i.e.*, a nanoreactor, Fig. 1a). Complete conversion requires an abundant amount of thiol groups in the droplet; thus, an equivalent thiol concentration (v/v% in ethanol) was selected on the basis of the Ag/S ratio, which can be determined *via* the equation

$$\frac{N_{Ag}}{N_S} = \frac{\frac{\pi\rho {D_p}^3}{6M_{Ag}}}{k_{max}\pi {D_p}^2} \quad (1)$$

where N_{Ag} and N_s are the atom numbers of Ag and S in a single Ag_2S nanodot, respectively, D_p is the mean size of a primary Ag particle, ρ is the density of Ag (10.49 g cm^{-3}), M_{Ag} is the atomic mass of Ag (107.87 g mol^{-1}), and k_{max} is the maximal factor for S coverage.

Scanning mobility particle sizer (SMPS, 3936, TSI, USA) measurements (Fig. S2a, ESI†) support the coexistence of Ag particles and thiols in a droplet, where the number of Ag particles represented in the size distribution curve decreases as the Ag particles combine with thiol droplets (*i.e.*, only the distribution of droplets remains). This quantitative incorporation between the Ag particles and thiol droplets occurs as they are sprayed through a collison atomizer (Fig. S1, ESI†). The conversion to Ag_2S nanodots is hypothesized to occur through the electrostatic interaction between the Ag particles and thiols, which is initiated by electron detachment (*i.e.*, photoionization) from Ag particles, where a photoionization rate [$\alpha(R_p)$] greater than zero is required. The photoionization rate under the present condition (6.4 s residence time) is determined using the equation

$$\alpha(R_p) = CI\frac{\pi {R_p}^2}{h\nu}\left[h\nu - \Phi_\infty - \frac{e^2}{4\pi\varepsilon_0 R_p}\left(q + \frac{3}{8}\right)\right]^2 \quad (2)$$

where C is the photoemission constant, I is the irradiation intensity, R_p is the particle radius, h is Planck's constant, ν is the photon's frequency, Φ_∞ is the work function of Ag, e is the elementary charge (1.602×10^{-19} C), ε_0 is the permittivity of vacuum (8.85×10^{-12} C^2 N^{-1} m^{-2}), and q is the initial number of charges. Given the dispersity of the Ag particles in the gas phase, the eventual surface charges of the Ag particles may induce antiagglomeration behavior because of their unipolar surface charges (*i.e.*, repulsive forces between the positively charged particles) during thiol incorporation. The mean posi-

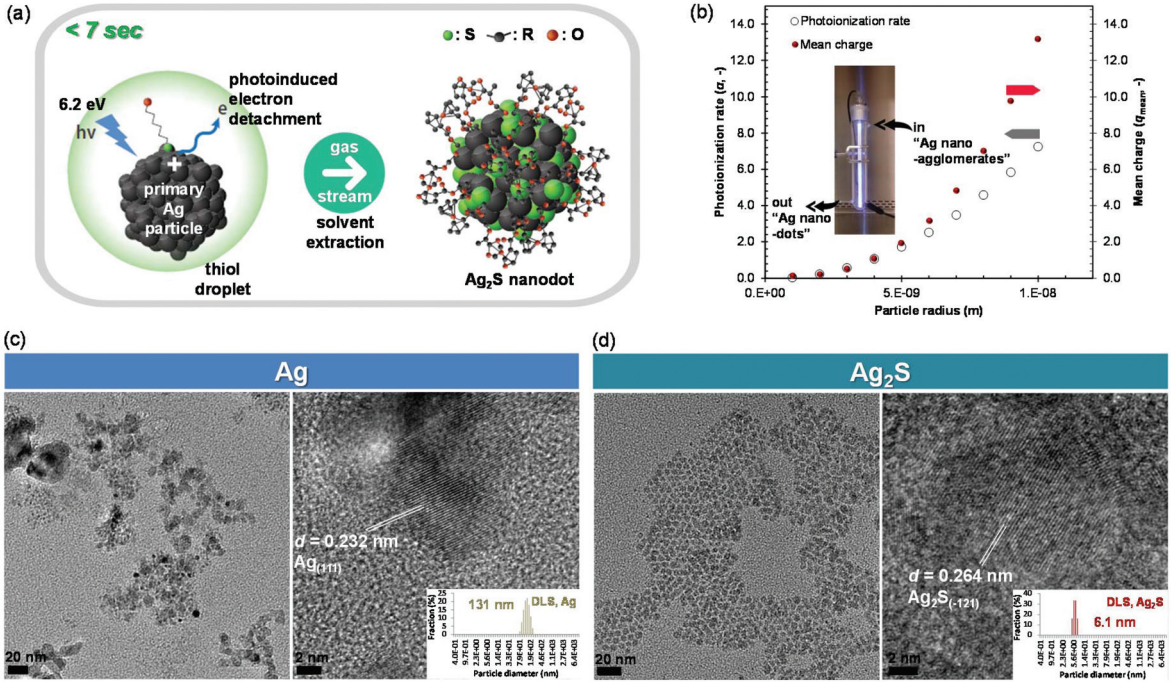

Fig. 1 (a) Schematic of the Ag_2S nanodot assembly process in a gas stream under photoirradiation (wavelength: 185 nm). A photon energy (6.2 eV) greater than the Ag work function (4.3 eV) induces electron detachment from the Ag surface; thus, positively charged surfaces subsequently interact with the negatively charged thiol groups in a thiol droplet. The continuous reaction in a fixed droplet residence time (~7 s) irradiation chamber leads to a complete surface coordination of Ag with thiols, resulting in the formation of Ag_2S. (b) Theoretical estimates of the photoionization rate and the mean charge (positive polarity) as a function of particle radius upon incidence of 185 nm UV light onto Ag nanoagglomerates. The results imply that the photoirradiation (inset) can derive a positively charged state of the Ag surface; thus, it is available to electrostatically interact with negatively charged thiol groups. Low- and high-magnification TEM images of (c) Ag nanoagglomerates and (d) Ag_2S nanodots after passing through a diffusion dryer. The right-side images of both samples include interplanar distances and DLS size distributions for samples in PBS. The nanoagglomerates are observed as bunches of primary Ag particles (~9.4 nm), whereas nanodots display an aligned structure of Ag_2S dots (restructured particle size: ~6.1 nm). In the case of DLS measurements, a significant difference is observed between the sizes of particles because of the agglomerated and unfunctionalized Ag nature.

tive charge of an Ag particle $[q_{\mathrm{mean}}(R_{\mathrm{p}}, t)]$ is estimated *via* the equation

$$q_{\mathrm{mean}}(R_{\mathrm{p}}, t) = \frac{\mathrm{CI}}{h\nu}\pi\left[R_{\mathrm{p}}(h\nu - \Phi_{\infty})\right]^2 t \qquad (3)$$

where t is the UV exposure time. Fig. 1b also shows the estimated numbers of positive charges as a function of particle size, and these results imply that continuous conversion from Ag to Ag_2S may occur in the photoirradiation chamber without substantial agglomeration. Transmission electron microscopy (TEM, Tecnai G^2 F20 S-TWIN, FEI, USA) observations (Fig. 1c) clearly validate the conversion from Ag nanoagglomerates into Ag_2S nanodots. The interplanar spacing (right-side TEM image) of particles from the photoinduced reaction increased to 0.264 nm from 0.234 nm [Miller (111) face-centered-cubic plane of Ag], which is matched to the (−121) planes of the monoclinic Ag_2S as well as to the bond-length range (0.237–0.280 nm) for silver–thiolate interactions.[12] X-ray diffraction (XRD, D/MAX-2500, Rigaku, Japan) measurements (Fig. S2b, ESI†) further supported the TEM analyses regarding the crystalline conversion. The size of the nanodots is uniform within the aligned structure, although upcoming Ag particles are agglomerated and the primary Ag particles are not monodisperse. The size and alignment of nanodots could be varied by modulating UV exposure time (Fig. S2c, ESI†), and the results showed that longer exposure times induced smaller sizes with uniform alignment due to higher mean positive charges (refer to eqn (3)) that prevents particle aggregation *via* electrostatic repulsive forces. These results indicate that the proposed route is suitable for the continuous conversion in a single-pass gas stream.

As shown in Fig. S2d (ESI†), X-ray photoelectron spectra (K-Alpha, Thermo Scientific, USA) further support the photoinduced changes in the surface composition and the valence state of the Ag and S in the Ag_2S nanodots. The shift in the binding energies of Ag confirms the presence of ionic Ag^+ (oxidized state) instead of metallic Ag, and the appearance of the S 2p peak at 166.8 eV implies the formation of Ag_2S with R–O–SH groups.[7] In addition, elemental analyses from the X-ray photoelectron spectroscopy (XPS) measurements demonstrate that the Ag/S atomic ratio in the Ag_2S nanodots is 1.8, which is stoichiometrically consistent with bulk Ag_2S.

The results of dynamic light scattering (DLS, Nano ZS90, Malvern Instruments, Ltd, UK) measurements of the Ag_2S

nanodots dispersed in phosphate-buffered saline (PBS, the inset of Fig. 1c) are consistent with the TEM observations, and their size distribution was maintained after 2 months of storage. These results imply that constant photoirradiation can continue the electrostatic reaction and that surface thiolates (negative charges) can thus be subsequently linked after the conversion is completed, leading to a uniform size distribution with an aligned structure. This implication is verified by the prominent peaks at approximately 2350 cm^{-1} in the Fourier transform infrared (FTIR, Nicolet iS10, ThermoFisher Scientific, USA) spectrum as shown in Fig. S2e (ESI†). These peaks are attributed to S–H stretching vibrations.[23] The small peak observed at approximately 1720 cm^{-1} corresponds to thiocarboxylate formed through oxidative chemisorption of ethanolic hexanethiol by photoionized Ag.[25] These results support the hypothesis that thiols in the droplet can act not only as a source of S to form Ag_2S but also act as a surfactant (*i.e.*, surface thiolates) to prevent unwanted agglomeration.[16,26] Analogous results were also achieved for different metal particles (from Pb or Cd to PbS or CdS with surface thiolates) under identical photoirradiation conditions (Fig. S3 and S4, ESI†), confirming that the proposed route can be extensively employed for the efficient assembly of metal sulfide nanodots.

However, the size of the Ag nanoagglomerates dispersed in PBS was substantially larger than that in the gas phase (Fig. S2a, ESI†) because of the lack of surface functional groups, which led to further agglomeration in the PBS.

The conversion to Ag_2S was also confirmed by UV-vis spectrophotometry (T60, PG Instruments, UK) by comparing the absorbances of particles before and after the photoinduced reaction (Fig. 2a). The spectrum of particles before the reaction reveals a typical surface plasmonic resonance for Ag NPs at 440 nm. Interestingly, the spectrum of particles after the reaction did not show a distinct absorption peak, possibly because the surface thiolates were sufficient to dampen the collective oscillation of conduction-band electrons (*i.e.*, convoluted inhomogeneity). These results are consistent with the chemisorption of thiols into Ag vacancies on the Ag NPs[27,28] and further support the phase transfer of Ag to Ag_2S with surface thiolates.

The inset of Fig. 2a depicts the PL spectrum of particles after the reaction, as recorded at room temperature using a fluorescence spectrophotometer (Fluoromax-4, Horiba, Japan) with excitation using a 785 nm laser diode. The emission peak is symmetric and centered at 1140 nm, with a full-width at half-maximum (FWHM) of 160 nm. The large FWHM might be

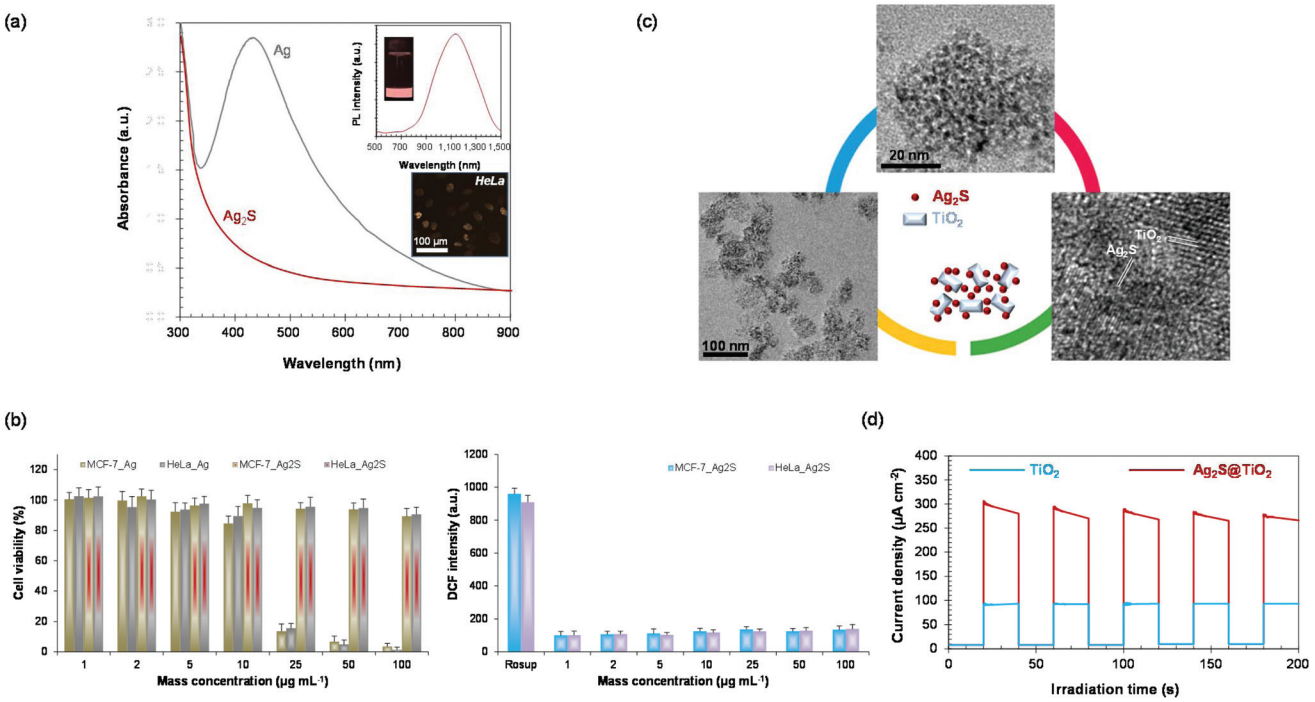

Fig. 2 (a) UV-vis spectra of Ag nanoagglomerates and Ag_2S nanodots. The inset shows the PL spectrum of Ag_2S nanodots and the PL image of an Ag_2S suspension in the presence of NIR (808 nm) radiation. Another inset shows an *in vitro* cellular PL image (800–1500 nm) of HeLa cells treated with an Ag_2S suspension. The bioactivities of Ag nanoagglomerates and Ag_2S nanodots on MCF-7 and HeLa cells. (b) Cytotoxicities (left) and intracellular ROS (right) of the cells treated with the different particles. All assays were conducted in a concentration-dependent manner and were performed in triplicate (n = 3). The p values were <0.05 and were thus regarded as statistically significant. (c) Low- and high-magnification TEM images of Ag_2S@TiO_2 nanocomposites for photocurrent generation. Flame-synthesized TiO_2 NPs were incorporated with Ag_2S nanodots in a gas stream, resulting in "bunch-like" nanocomposites. The self-assembled nanocomposites were then deposited in a thermophoretic manner onto a substrate to be exposed to simulated solar light. (d) Transient photocurrent responses of TiO_2 and Ag_2S@TiO_2 samples under constant solar irradiation (100 mW cm^{-2}).

attributable to the aligned structure of Ag_2S with surface thiolates. The dispersion in PBS under laser irradiation exhibits bright IR luminescence; thus, the second NIR window (NIR-II, 1.0–1.4 μm) emission is promising as a fluorescent probe in bioimaging because it reduces background autofluorescent noises.[10]

To demonstrate the feasibility of Ag_2S nanodots as fluorescent probes, we used a fluorescence microscope (BX51, Olympus, Japan) to visualize HeLa cells incubated with the nanodots for 24 h, as shown by reddish signals with low fluorescence backscattering (another inset of Fig. 2a), demonstrating NIR PL signals (red–white).[10] The PL lifetime was determined by recording PL decays at 380 nm laser excitation, and average lifetime was 969 ns. This is comparable to previous reports[29,30] and thus, may warrant further investigation in bioimaging applications. The quantum yield of the nanodots was found to be 4.2%, which is substantially higher than the quantum yield of IR-26 NIR standard dye (0.5% quantum yield). To confirm the biocompatibility of nanodots, we investigated the cytotoxicity and ROS generation in MCF-7 and HeLa cells after 24 h of incubation with the nanodots and compared the results with those for MCF-7 and HeLa cells after 24 h incubation with the Ag nanoagglomerates (Fig. 2b). The average cell viabilities after exposure to the nanodots remained greater than 85% in the tested concentration range from 1 to 100 μg mL^{-1}. By contrast, the Ag nanoagglomerates exhibited significant cytotoxicities (>80% cell death) in both cell lines at concentrations greater than 25 μg mL^{-1}. The lack of significant cytotoxicity of the nanodots may be due to the very low solubility ($K_{sp} = 6.3 \times 10^{-50}$) of Ag_2S at 25 °C, which prevents the substantial release of Ag^+ ions into the cells.[10]

The generation of ROS in MCF-7 and HeLa cells induced by incubating the cells with the nanodots for 24 h was also determined by monitoring fluorescent 2′,7′-dichlorofluorescein (DCF). Oxidative stress is an indicator of redox imbalance in cells because of increased intracellular generation of ROS, which can cause DNA damage, necrosis, and cell death. At all of the tested concentrations (1–100 μg mL^{-1}), the nanodots induced a negligible amount of ROS compared with a Rosup-treated positive control. No significant statistical variation was observed for either cell line treated with the nanodots. Given the results from both cytotoxicity assays, the nanodots may be suitable for bioimaging, exhibiting no significant cytotoxicity issues at concentrations as high as 100 μg mL^{-1}. Fluorescence bioimaging with no significant cytotoxicities was also achieved for other nanodots (PbS and CdS, Fig. S5, ESI†), which demonstrates the potential of the developed method for generalizable use in fluorescence bioimaging.

Hemolysis assay (Fig. S6, ESI†) further supports the differences between Ag and Ag_2S in cytotoxicity and ROS generation. The Ag_2S nanodots did not show significant hemolysis (<4%) where they co-incubated with red blood cells with different concentrations (10–100 μg mL^{-1}) while the result for Ag reached about 48% at 100 μg mL^{-1}. This suggests that the single-pass process may be suitable to confer biocompatibility and hemoprotective properties for biological applications.

As a significant extending application of the nanodots, the nanodots were incorporated with TiO_2 NPs (*i.e.*, Ag_2S@TiO_2 nanocomposites) to evaluate photocurrent generation under simulated solar irradiation because IR radiation represents approximately 70% of the photon flux of the entire solar spectrum.[31] To prepare Ag_2S@TiO_2 nanocomposites in a single-pass gas stream, we injected ultrasonic-flame-synthesized TiO_2 NPs[32] into Ag_2S nanodots flowing under an alternating electric field (2.5 kV cm^{-1}, 1 kHz), where they were charged with gaseous positive ions to facilitate their efficient merging with the nanodots (refer to the ESI†). Low- and high-magnification TEM images (Fig. 2c) of the nanocomposites demonstrate that the Ag_2S and TiO_2 coexisted in a bunch-like nanocomposite. Spatial elemental analysis of the composite film was performed using scanning electron microscopy (SEM, JSM-6500F, JEOL, Japan) and energy-dispersive X-ray (EDX, JED-2300, JEOL, Japan) measurements (Fig. S7, ESI†). The ratio between Ag_2S and TiO_2 was 28.8 : 71.2, and the atomic fractions between Ag (or Ti) and S (or O) were matched to Ag_2S (or TiO_2), implying that the single-pass process can be extended to assemble equivalent nanocomposites. Measurements of transient photocurrent generated by the nanocomposites (Fig. 2d) under simulated solar irradiation in an on–off configuration revealed a current density approximately three times greater than that achieved using TiO_2 NPs alone. This enhancement may originate from the construction of nanocomposites that improve the photoactivity of TiO_2 by broadening and red-shifting its bandgap through the separation of photoexcited electron–hole pairs mediated by new propagation pathways for photoelectrons [Ag_2S (h^+) + TiO_2 (e^-) → Ag_2S + TiO_2].[33] Increased electrical conductivity and mobility resulting from the Ag_2S incorporation may also contribute to the enhancement of TiO_2 photoactivity. Incident photon-to-current efficiency (IPCE, Fig. S8, ESI†)[34] of Ag_2S@TiO_2 solar cells was further measured to demonstrate an extension of the single-pass process. A significant enhancement in IPCE even at longer wavelengths (>600 nm) for Ag_2S@TiO_2 compared to TiO_2 is due to a broadband absorption after TiO_2 nanoparticles were incorporated with Ag_2S nanodots that facilitates interparticle plasmonic coupling between the adjacent Ag_2S nanodots or Ag_2S nanodots and TiO_2 nanoparticles (*i.e.*, enhancing photocurrent generation in the solar cells). The observed improvements in photoactivity support another potential application of the proposed route: efficient light-harvesting.

Conclusions

Continuous conversion of Ag to Ag_2S with surface thiolates was achieved *via* the assembly of hybrid droplets comprising Ag nanoagglomerates and thiols and subsequent 185 nm UV irradiation for less than 7 s in an ambient single-pass gas stream. Photoionization of Ag initiated the electrostatic incorporation of thiols and led to the preparation of crystalline Ag_2S nanodots without a conventional hydrothermal or vacuum

reaction with complex controls. The surface thiolates prevented unwanted agglomeration; thus, an aligned structure was obtained by overcoming significantly faster particle kinetics in the gas phase than that in the liquid phase. The nanodots did not show significant cytotoxicity or oxidative stress and were feasible for NIR-induced fluorescence bioimaging. Furthermore, a single-pass incorporation of the nanodots with TiO_2 NPs was suitable to enhance the photocurrent generation capability of TiO_2 under simulated solar irradiation. These findings confirm the validity of the photoinduced conversion of agglomerated Ag into aligned crystalline Ag_2S, demonstrating a novel safe-by-design route for assembling various sulfide nanodots for biological and energy-conversion applications.

Conflicts of interest

There are no conflicts to declare.

Acknowledgements

This work was supported by the National Research Foundation of Korea Grant funded by the Korean Government (NRF-2015R1A2A2A04005809). This work was also supported by the 214A054039 Yeungnam University Research Grant.

Notes and references

1 P. Liu, R. Qin, G. Fu and N. Zheng, *J. Am. Chem. Soc.*, 2017, **139**, 2122.
2 X. Liu, Y. Yang and M. W. Urban, *Macromol. Rapid Commun.*, 2017, **38**, 1700030.
3 G. Paramasivam, N. Kayambu, A. M. Rabel, A. K. Sundramoorthy and A. Sundaramurthy, *Acta Biomater.*, 2017, **49**, 45.
4 X. Bai, F. Liu, Y. Liu, C. Li, S. Wang, H. Zhou, W. Wang, H. Zhu, D. A. Winkler and B. Yan, *Toxicol. Appl. Pharmacol.*, 2017, **323**, 66.
5 H. Naatz, S. Lin, R. Li, W. Jiang, Z. Ji, C. H. Chang, J. Köser, J. Thöming, T. Xia, A. E. Nel, L. Mädler and S. Pokhrel, *ACS Nano*, 2017, **11**, 501.
6 E. Burello and A. P. Worth, *Nanotoxicology*, 2015, **9**, 116.
7 Y. Feng, Q. Yao, J. Li, N. Goswami, J. Xie and J. Yang, *Nano Res.*, 2016, **9**, 942.
8 J. Liu, P. N. Duchesne, M. Yu, X. Jiang, X. Ning, R. D. Vinluan III, P. Zhang and J. Zheng, *Angew. Chem., Int. Ed.*, 2016, **55**, 8894.
9 L. Gong, Y. Wang and J. Liu, *Biomater. Sci.*, 2017, **5**, 1393.
10 Y. Zhang, G. Hong, Y. Zhang, G. Chen, F. Li, H. Dai and Q. Wang, *ACS Nano*, 2012, **6**, 3695.
11 C. Battocchio, C. Meneghini, I. Fratoddi, I. Venditti, M. V. Russo, G. Aquilanti, C. Maurizio, F. Bondino, R. Matassa, M. Rossi, S. Mobilio and G. Polzonetti, *J. Phys. Chem. C*, 2012, **116**, 19571.
12 Y. Liu, B. K. Najafabadi, M. A. Fard and J. F. Corrigan, *Angew. Chem., Int. Ed.*, 2015, **54**, 4832.
13 H. Hinterwirth, S. Kappel, T. Waitz, T. Prohaska, W. Lindner and M. Lämmerhofer, *ACS Nano*, 2013, **7**, 1129.
14 T. Yang, Y. Tang, L. Liu, X. Lv, Q. Wang, H. Ke, Y. Deng, H. Yang, X. Yang, G. Liu, Y. Zhao and H. Chen, *ACS Nano*, 2017, **11**, 1848.
15 L. Tan, A. Wan and H. Li, *ACS Appl. Mater. Interfaces*, 2013, **5**, 11163.
16 I. Chakraborty and T. Pradeep, *Chem. Rev.*, 2017, **117**, 8208.
17 J. H. Byeon, J. H. Park, K. Y. Yoon and J. Hwang, *Nanoscale*, 2009, **1**, 339.
18 J. Feng, G. Biskos and A. Schmidt-Ott, *Sci. Rep.*, 2015, **5**, 15788.
19 X. Zhai, S. Li, Y. Ding, L. Pan, H. Yang, B. Jiang, D. Yan and Q. Meng, *J. Nanomater.*, 2016, **2016**, 4363541.
20 X. Fang, X. Yang and D. Yan, *J. Mater. Chem. C*, 2017, **5**, 1632.
21 E.-H. Kong, Y.-J. Chang, H.-J. Park and H. M. Jang, *Small*, 2014, **10**, 1300.
22 B. Liu, D. Wang, Y. Zhang, H. Fan, Y. Lin, T. Jiang and T. Xie, *Small*, 2013, **42**, 2232.
23 D. Asik, M. B. Yagci, F. D. Duman and H. Y. Acar, *J. Mater. Chem. B*, 2016, **4**, 1941.
24 Y. Cao, W. Geng, R. Shi, L. Shang, G. I. N. Waterhouse, L. Liu, L.-Z. Wu, C.-H. Tung, Y. Yin and T. Zhang, *Angew. Chem., Int. Ed.*, 2016, **55**, 14952.
25 J. H. Byeon and J. T. Roberts, *Chem. Mater.*, 2012, **24**, 3544.
26 H. D. A. Santos, D. Ruiz, G. Lifante, C. Jacinto, B. H. Juarez and D. Jaque, *Nanoscale*, 2017, **9**, 2505.
27 H. Doh, S. Hwang and S. Kim, *Chem. Mater.*, 2016, **28**, 8123.
28 M. R. Branham, A. D. Douglas, A. J. Mills, J. B. Tracy, P. S. White and R. W. Murray, *Langmuir*, 2006, **22**, 11376.
29 Y. Wang and X.-P. Yan, *Chem. Commun.*, 2013, **49**, 3324.
30 X. Jia, D. Li, J. Li and E. Wang, *RSC Adv.*, 2015, **5**, 80929.
31 C. Ji, Y. Zhang, X. Zhang, P. Wang, H. Shen, W. Gao, Y. Wang and W. W. Yu, *Nanotechnology*, 2017, **28**, 065602.
32 G. W. Lee and J. H. Byeon, *Mater. Charact.*, 2009, **60**, 1476.
33 S. Cheng, W. Fu, H. Yang, L. Zhang, J. Ma, H. Zhao, M. Sun and L. Yang, *J. Phys. Chem. C*, 2012, **116**, 2615.
34 Y. Tang, W. He, Y. Lu, J. Fielden, X. Xiang and D. Yan, *J. Phys. Chem. C*, 2014, **118**, 25365.